Computer Physics Communications 307 (2025) 109432

Contents lists available at ScienceDirect

Computer Physics Communications

journal homepage: www.elsevier.com/locate/cpc

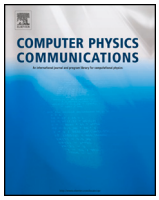

Computational Physics

# Robust spectral proper orthogonal decomposition ☆

Antonio Colanera [a,b,*], Oliver T. Schmidt [c], Matteo Chiatto [a]

[a] Department of Industrial Engineering, University of Naples "Federico II", P.le tecchio 80, Naples, 80125, Italy
[b] Department of Mechanical and Aerospace Engineering, Politecnico di Torino, Corso Duca degli Abruzzi 24, Turin, 10129, Italy
[c] Department of Mechanical and Aerospace Engineering, University of California San Diego, La Jolla, CA, USA

ARTICLE INFO

*Keywords:*
Low-dimensional models
Modal analysis
Turbulent flows

ABSTRACT

Experimental measurements often present corrupted data and outliers that can strongly affect the main coherent structures extracted with the classical modal analysis techniques. This effect is amplified at high frequencies, whose corresponding modes are more susceptible to contamination from measurement noise and uncertainties. Such limitations are overcome by a novel approach proposed here, the robust spectral proper orthogonal decomposition (robust SPOD), which implements the robust principal component analysis within the SPOD technique. The new technique is firstly presented with details on its algorithm, and its effectiveness is tested on two different fluid dynamics problems: the subsonic jet flow field numerically simulated, and the flow within an open cavity experimentally analyzed in [48]. The analysis of the turbulent jet data, corrupted both with salt and pepper and Gaussian noise, shows how the robust SPOD produces more converged and physically interpretable modes than the classical SPOD; moreover, the use of the robust SPOD as a tool for de-noising data, based on the signal reconstruction from de-noised modes, is also presented. Applying robust SPOD to the open cavity flow has revealed that it yields smoother spatial distributions of modes, particularly at high frequencies and when considering higher-order modes, compared to standard SPOD.

## 1. Introduction

Data corruption is a significant obstacle to systems modeling and forecasting; noisy and gappy measurements can severely affect the learned models and lead to invalid conclusions. The ability to handle this data type has a significant role in developing reduced-order models (ROMs) and in the inference of physical insights from experimental investigations.

A typical way to obtain a ROM is to extract physically important features or modes that characterize the flow topology and project the Navier-Stokes equations (Galerkin projection) onto a subset of these modes, resulting in a system of ordinary differential equations, [28]. Choosing a restricted set of modes among those available makes it possible to build a reduced model that can predict the flow field behavior with a lower computational cost. In particular, different techniques can be used to obtain the main flow coherent structures [32,41], which may suffer the presence of outliers and gappy data.

In recent studies, variational autoencoder architectures combined with transformers have demonstrated potential in developing compact and near-orthogonal reduced-order models for chaotic fluid flows, showcasing improved interpretability and prediction performance over traditional methods [38].

Among the modal analysis techniques, spectral proper orthogonal decomposition (SPOD) has gained much interest in the last years due to its ability to extract the main spectral features of a flow field, optimally capturing the two-point space–time correlations, thus providing modes that evolve coherently in space and time [34,42,35]. SPOD algorithm has been employed in various fluid dynamics applications, mainly for post-processing numerical and experimental data. This technique is a valuable tool to investigate the flow topology itself [8,6,10,27,15,9,1] and even to evaluate the flow receptivity and the effectiveness of an applied control strategy [7].

Nowadays, one of the most used experimental measurement techniques is the particle image velocimetry (PIV), which can suffer from erroneous measurements due to inadequate illumination, optical issues, reflections, and sharp gradients in field properties [17]. Experimental measurements have to deal with the trade-off between the quantity and quality of PIV data; thus, acquired flow fields often have corrupt

☆ The review of this paper was arranged by Prof. Peter Vincent.

* Corresponding author.
*E-mail address:* antonio.colanera@unina.it (A. Colanera).

https://doi.org/10.1016/j.cpc.2024.109432
Received 2 February 2024; Received in revised form 24 July 2024; Accepted 11 November 2024
Available online 15 November 2024

and even missing measurements. Standard filtering and reconstruction techniques involve interpolation methods that rely only on local flow information [45], least square methods, and Kriging [29].

The problem of gappy measurements has traditionally been addressed with approaches based on proper orthogonal decomposition, POD, [12,43,14]. Recently, Nekkanti and Schmidt [26] have demonstrated the gappy SPOD capability in reconstructing flow fields. Even machine learning techniques such as Physics-informed neural networks, PINNs [44], long short-term memory (LSTM) networks [49], deep generative adversarial model, deep generative adversarial model, deep-GAN [4] and autoencoders [11] can be efficiently employed to generate missing data in turbulence and processing PIV data.

On the other hand, the problem of the presence of outliers in data whose location is not known a priori was efficiently faced using matrix completion, which separates the sparse noise from the data [5] through different algorithmic approaches such as augmented Lagrange multiplier (ALM) and alternating directions method (ADM) ([47] and [21]). These techniques have been proven helpful for experimental data post-processing and modal decompositions [33].

### 1.1. Aim and organization of the paper

The algorithm of the SPOD technique represents the frequency domain version of the standard space-only POD [19], which is not robust to outliers and corrupted data. This work aims to overcome this limitation by introducing the robust spectral proper orthogonal decomposition (robust SPOD) and describing its algorithm in detail. The technique is applied to classical fluid dynamics problems to analyze different aspects of the algorithm: the subsonic jet flow field numerically computed by large-eddy simulations (LES) from [34] and the flow within an open cavity, obtained using PIV measurements from [48].

The work is organized as follows. In section 2, we review the standard and gappy SPOD technique and then introduce the robust SPOD procedure. Section 3 describes two different test cases used to evaluate the performances of the robust SPOD technique; finally, the results are reported in section 4.

## 2. Methodology

### 2.1. Standard SPOD

Following the works of Towne et al. [42] and Schmidt and Colonius [36], the standard SPOD algorithm is briefly summarized here. Let the snapshots ensemble $\{\boldsymbol{q}_i\}$ be the collection of instantaneous states of a generic field $\boldsymbol{q}(\boldsymbol{x},t)$, defined in the space $\boldsymbol{x}$ at time $t_i$ (with $i=1,...,M$), organized to form a data matrix $\boldsymbol{Q}\in\mathbb{R}^{N\times M}$, being $N$ the total length of the vector equal to the number of grid points times the number of flow variables. The data matrix $\boldsymbol{Q}$ is then divided into $N_b$ blocks $\mathbf{Q}^{(j)}$, with $j$ running from 1 to $N_b$, composed of $N_f$ snapshots, even overlapping each other; the number of overlapped snapshots is $N_o$. For each block, a (windowed) discrete Fourier transform (FFT) is computed. Each block-wise Fourier component realization is stacked in a matrix $\hat{\mathbf{Q}}_{f_k}\in\mathbb{R}^{N\times N_b}$ for each frequency $f_k$, with $k=1,...,N_f$, and then a standard POD decomposition is carried out on these matrices, namely an eigenvalue decomposition of the cross-spectral density (CSD) matrix

$$\mathbf{S}_{f_k}=\hat{\mathbf{Q}}_{f_k}\hat{\mathbf{Q}}^{*}_{f_k}\boldsymbol{W}, \tag{1}$$

in which $\boldsymbol{W}$ is a spatial weight matrix considering the data's non-uniformity, see, e.g., [36]. With such decomposition SPOD modes correspond to the columns of the matrix $\boldsymbol{\Phi}_{f_k}\in\mathbb{C}^{N\times N_b}$ and are ranked according to their corresponding eigenvalues given by the matrix $\boldsymbol{\Lambda}_{f_k}\in\mathbb{C}^{N\times N}$.

The problem (1) is frequently replaced by the smaller eigenvalue problem (snapshots method)

$$\hat{\mathbf{Q}}^{*}_{f_k}\boldsymbol{W}\hat{\mathbf{Q}}_{f_k}\boldsymbol{\Psi}_{f_k}=\boldsymbol{\Psi}_{f_k}\widetilde{\boldsymbol{\Lambda}}_{f_k}, \tag{2}$$

where $\widetilde{\boldsymbol{\Lambda}}_{f_k}\in\mathbb{C}^{N_b\times N_b}$ are the non-zero eigenvalues of (1), whereas the eigenvectors are $\boldsymbol{\Phi}_{f_k}=\hat{\mathbf{Q}}_{f_k}\boldsymbol{\Psi}_{f_k}\widetilde{\boldsymbol{\Lambda}}^{-1/2}_{f_k}$.

A low-rank field reconstruction can be obtained (either in frequency or in the temporal domain) considering a certain number of SPOD modes, as shown by Nekkanti and Schmidt [25].

### 2.2. Gappy SPOD

Recently Nekkanti and Schmidt [26] have developed an algorithm dealing with gappy data. Similarly to the standard SPOD procedure, the first step is to divide the time series into some blocks and then compute the Fourier components realizations for each block (because of the gaps, an FFT algorithm that can deal with a nonuniform temporal sampling must be employed). Considering the $k^{th}$ gap, the procedure computes SPOD modes by employing only blocks unaffected by this gap. Once this SPOD basis has been computed, SPOD expansion coefficients for blocks affected by the $k^{th}$ gap are calculated, projecting the Fourier components realizations on this basis. Finally, with known SPOD basis and expansion coefficients, it is possible to reconstruct the flow field, also filling the gap, through an inverse Fourier transform (IFFT). The convergence of the $k^{th}$ gap is evaluated by means of the parameter:

$$c_n=\sum_{i\in G_n}\frac{\|\tilde{\boldsymbol{q}}^{g^j}_i-\tilde{\boldsymbol{q}}^{g^{j-1}}_i\|^2_2}{\|\tilde{\boldsymbol{q}}^{g^{j-1}}_i\|^2_2}, \tag{3}$$

in which $G_n$ is the snapshot ensemble affected by $n^{th}$ gap, $\tilde{\boldsymbol{q}}^{g}$ represents the reconstructed data in the gappy regions only, and superscript $j$ is the iteration index. The procedure must be repeated for all the gaps until global convergence is reached.

This technique is effective but assumes that gaps and corrupted data location are known *a priori*.

### 2.3. Robust SPOD

SPOD algorithm, as seen in the section 2.1, is based on the eigenvalue decomposition of the CSD matrix. In this way, if the original data include outliers, the latter will be retrieved (and even amplified) in the Fourier realizations, leading to corrupted and noisy modes. To avoid this occurrence, we propose using the robust PCA within the SPOD technique, introduced by Candes et al. [5] and reviewed by Scherl et al. [33].

Specifically, we present two distinct procedures: one applies robust PCA to the Fourier realization $\hat{\mathbf{Q}}_{f_k}$, while the other directly applies it to the snapshots blocks $\mathbf{Q}^{(j)}$. The features and algorithms of these procedures will be discussed in detail hereafter.

The robust PCA can be used to decompose the matrix of the Fourier realizations $\hat{\mathbf{Q}}_{f_k}$ (or equivalently the snapshots blocks $\mathbf{Q}^{(j)}$), into

$$\hat{\mathbf{Q}}_{f_k}=\hat{\mathbf{L}}_{f_k}+\hat{\mathbf{H}}_{f_k}, \tag{4}$$

with $\hat{\mathbf{L}}_{f_k}$ being a low rank structure and $\hat{\mathbf{H}}_{f_k}$ a sparse matrix containing outliers and corrupted data, [5]. In this way, the principal components of $\hat{\mathbf{L}}_{f_k}$ would not be affected by the presence of the incorrect data. To highlight how the robust PCA isolates outliers into the matrix $\hat{\mathbf{H}}_{f_k}$, it is insightful to consider that, for the standard POD, the mathematical problem for the extraction of the desired low rank ($r$) structures $\hat{\mathbf{L}}_{f_k}$ consists in the minimization of the Frobenius norm ($\|\cdot\|_F$) of the term $\hat{\mathbf{H}}_{f_k}=\hat{\mathbf{Q}}_{f_k}-\hat{\mathbf{L}}_{f_k}$:

$$\min_{\hat{\mathbf{L}}_{f_k}}\|\hat{\mathbf{Q}}_{f_k}-\hat{\mathbf{L}}_{f_k}\|_F\quad\text{subject to}\quad\text{rank}(\hat{\mathbf{L}}_{f_k})\le r. \tag{5}$$

The choice of the Frobenius norm makes the computation results highly sensitive to outliers.

For the robust PCA, instead, the optimization problem consists in:

$$\min_{\hat{\mathbf{L}}_{f_k},\hat{\mathbf{H}}_{f_k}}\text{rank}(\hat{\mathbf{L}}_{f_k})+\|\hat{\mathbf{H}}_{f_k}\|_0\quad\text{subject to}\quad\hat{\mathbf{L}}_{f_k}+\hat{\mathbf{H}}_{f_k}=\hat{\mathbf{Q}}_{f_k}, \tag{6}$$

in which $\|\hat{\mathbf{H}}_{f_k}\|_0$ is the cardinality of nonzero elements in $\hat{\mathbf{H}}_{f_k}$ (featuring the sparsity of $\hat{\mathbf{H}}_{f_k}$). Problem (6) is non convex and typically is solved considering its *convex relaxation* [5]:

$$\min_{\hat{\mathbf{L}}_{f_k},\hat{\mathbf{H}}_{f_k}} \|\hat{\mathbf{L}}_{f_k}\|_* + \alpha_0\|\hat{\mathbf{H}}_{f_k}\|_1 \quad \text{subject to} \quad \hat{\mathbf{L}}_{f_k} + \hat{\mathbf{H}}_{f_k} = \hat{\mathbf{Q}}_{f_k}, \tag{7}$$

in which $\|\cdot\|_*$ is the nuclear norm (i.e., the sum of the singular values) and $\|\cdot\|_1$ is the $L_1$ norm (i.e., the sum of the magnitudes of each entry in the matrix). The coefficient $\alpha_0$ is defined as,

$$\alpha_0 = \alpha/\sqrt{\max(N, N_b)}, \tag{8}$$

where $\alpha$ has to be tuned and represents the filter intensity [33].

The problem (7) is known as *principal component pursuit* and may be solved using the augmented Lagrange multiplier (ALM) algorithm, see [21] and [47]. Following Candes et al. [5], in this work, the augmented Lagrangian has been defined as:

$$\ell(\hat{\mathbf{L}}_{f_k}, \hat{\mathbf{H}}_{f_k}, \mathbf{Y}) = \|\hat{\mathbf{L}}_{f_k}\|_* + \alpha_0\|\hat{\mathbf{H}}_{f_k}\|_1 + \langle \mathbf{Y}, \hat{\mathbf{Q}}_{f_k} - \hat{\mathbf{L}}_{f_k} - \hat{\mathbf{H}}_{f_k}\rangle + \frac{\mu}{2}\|\hat{\mathbf{Q}}_{f_k} - \hat{\mathbf{L}}_{f_k} - \hat{\mathbf{H}}_{f_k}\|_F, \tag{9}$$

in which $\mathbf{Y}$ is the matrix of Lagrange multipliers, $\langle\cdot,\cdot\rangle$ is the standard trace inner product and $\mu$ a parameter that counts the error in (4). In this work, the relaxation parameter $\mu$ has been chosen according to $\mu = 0.25 N N_b/\|\hat{\mathbf{Q}}_{f_k}\|_1$. It is worth noticing that $\mu$ does not affect the solution of the problem (6) but only the convergence speed. The set of $(\hat{\mathbf{L}}_{f_k}, \hat{\mathbf{H}}_{f_k}, \mathbf{Y})$ that minimizes the (9) can be found in different ways, as reported in [5], [21] and [47]. In the present work the alternating directions method (ADM) has been employed. Once the robust PCA algorithm converges, the so-obtained de-noised Fourier realizations matrix $\hat{\mathbf{L}}_{f_k}$ is employed instead of $\hat{\mathbf{Q}}_{f_k}$ in the standard SPOD procedure.

In case of the application of robust PCA directly on the snapshots blocks $\mathbf{Q}^{(j)}$, it extracts the low-rank blocks matrices $\mathbf{L}^{(j)}$ and the sparse matrices $\mathbf{H}^{(j)}$ containing the noise. In this case, the denoised matrices $\mathbf{L}^{(j)}$ are employed for the computation of the CSD matrix following the standard SPOD algorithm.

It is worth noting that the standard ADM method deals with real matrices, whereas in the case of the procedure considering the decomposition of the matrices $\hat{\mathbf{Q}}_{f_k}$ it has to deal with complex matrices. For this reason shrinkage operator $\mathcal{S}$ is not defined as usual with $\mathcal{S}(\tau, \mathbf{B}) = \text{sign}(\mathbf{B})\max(|\mathbf{B}| - \tau, 0)$ but as shown in the following Equation (10).

Both SPOD and Robust SPOD results rely on the accurate estimation of the CSD matrix, which is influenced not only by the quality of the data but also by the choice of various spectral estimation parameters present in the algorithms. For standard SPOD, there are different references that help in selecting these parameters, such as [36] and standard signal processing handbooks like [23] and [2]. In this work, we will focus on the choice of parameters for Robust SPOD, specifically the effect of $\alpha$ parameters will be studied.

The robust SPOD algorithms considered in this work are reported hereafter. Algorithm 1, shows the robust SPOD algorithm with denoising of the $\hat{\mathbf{Q}}_{f_k}$; the robust PCA procedure is reported in Algorithm 2, while Algorithm 3 illustrates the robust SPOD with principal component pursuit on each block.

### 2.3.1. Robust SPOD algorithms

In this section, the major features of the proposed methodology will be outlined.

The algorithm corresponding to the application of the robust PCA algorithm before those of the FFT, directly on matrices $\mathbf{Q}^{(j)}$ is reported in Algorithm 3. Indeed, if the FFT algorithm is carried out before the PCA, then the technique completely preserves the spectral information related to the dynamics occurring in small regions of the domain. On the contrary, applying the robust PCA technique before the FFT thoroughly filters the local dynamics.

**Algorithm 1** Robust spectral proper orthogonal decomposition algorithm.

1. For each data block $j = 1, ..., N_b$:
   (a) assemble data matrices
   $$\mathbf{Q}^{(j)} = \left[\boldsymbol{q}^{(j)}_{1+(j-1)(N_f-N_o)}, \boldsymbol{q}^{(j)}_{2+(j-1)(N_f-N_o)}, ..., \boldsymbol{q}^{(j)}_{N_f+(j-1)(N_f-N_o)}\right],$$
   with $N_o$ being the number of overlapping snapshots.
   (b) Within each block perform weighted FFT
   $$\hat{\mathbf{Q}}^{(j)} = \mathcal{F}\left\{\mathbf{Q}^{(j)}\boldsymbol{W}_T\right\},$$
   where $\boldsymbol{W}_T$ is the matrix of the window weights. Columns of $\hat{\mathbf{Q}}^{(j)}$, $\hat{\boldsymbol{q}}^{(j)}_k$ are the $j_{th}$ realizations of the Fourier mode at the $k^{th}$ discrete frequency $f_k$.
2. For each frequency $f_k$, with $k = 1, ..., N_f$:
   (a) Collect Fourier transform realizations in the matrices $\hat{\mathbf{Q}}_{f_k} = \sqrt{\kappa}\left[\hat{\boldsymbol{q}}^{(1)}_k, \hat{\boldsymbol{q}}^{(2)}_k, ..., \hat{\boldsymbol{q}}^{(N_b)}_k\right]$, where $\kappa = \Delta t/(N_b\|\boldsymbol{W}_T\|^2_F)$.
   (b) Split $\hat{\mathbf{Q}}_{f_k}$ in $\hat{\mathbf{L}}_{f_k}$ and $\hat{\mathbf{H}}_{f_k}$ with robust PCA algorithm (see Algorithm 2). Store $\hat{\mathbf{H}}_{f_k}$ if needed.
   (c) With the de-noised matrix $\hat{\mathbf{L}}_{f_k}$ calculate
   $$\mathbf{M}_{f_k} = \hat{\mathbf{L}}^*_{f_k}\mathbf{W}\hat{\mathbf{L}}_{f_k}.$$
   (d) Perform the eigendecomposition of $\mathbf{M}_{f_k}$
   $$\mathbf{M}_{f_k} = \boldsymbol{\Theta}_{f_k}\boldsymbol{\Lambda}_{f_k}\boldsymbol{\Theta}^*_{f_k}.$$
   For the $k^{th}$ frequency, store de-noised SPOD eigenvalues $\boldsymbol{\Lambda}_{f_k}$.
   (e) Compute de-noised SPOD modes for the $k^{th}$ frequency with
   $$\boldsymbol{\Phi}_{f_k} = \hat{\mathbf{L}}_{f_k}\boldsymbol{\Theta}_{f_k}\boldsymbol{\Lambda}^{-1/2}_{f_k}$$
3. Return $\boldsymbol{\Phi}_{f_k}$ and $\boldsymbol{\Lambda}_{f_k}$.

**Algorithm 2** Robust PCA algorithm with principal component pursuit by ADM (from [21] and [47]).

Given a matrix $\hat{\mathbf{Q}}_{f_k}$ and the parameters $\alpha_0$ and $\mu$:

1. Initialize matrices $\hat{\mathbf{H}}_{f_k}$, $\hat{\mathbf{L}}_{f_k}$ and Lagrange multipliers matrix $\mathbf{Y}$:
   $$\hat{\mathbf{H}}^i_{f_k} = \mathbf{0},$$
   $$\hat{\mathbf{L}}^i_{f_k} = \mathbf{0},$$
   $$\mathbf{Y}^i = \mathbf{0}.$$
2. Update matrices
   $$\hat{\mathbf{L}}^{i+1}_{f_k} = \mathcal{T}(1/\mu, \hat{\mathbf{Q}}_{f_k} - \hat{\mathbf{H}}^i_{f_k} - \mathbf{Y}^i/\mu),$$
   $$\hat{\mathbf{H}}^{i+1}_{f_k} = \mathcal{S}(\alpha_0/\mu, \hat{\mathbf{Q}}_{f_k} - \hat{\mathbf{L}}^{i+1}_{f_k} + \mathbf{Y}^i/\mu),$$
   $$\mathbf{Y}^{i+1} = \mathbf{Y}^i + \mu(\hat{\mathbf{Q}}_{f_k} - \hat{\mathbf{L}}^{i+1}_{f_k} - \hat{\mathbf{H}}^{i+1}_{f_k}),$$
   in which operator $\mathcal{T}$ is the singular value thresholding operator:
   $$\mathbf{A} = \mathcal{T}(\tau, \mathbf{B}) = \mathbf{U}\mathcal{S}(\tau, \mathbf{S})\mathbf{U}^H \quad \text{with} \quad [\mathbf{U}, \mathbf{S}, \mathbf{V}] = \text{svd}(\mathbf{B}),$$
   and $\mathcal{S}$ is the shrinkage operator defined as:
   $$\mathbf{A} = \mathcal{S}(\tau, \mathbf{B}) = e^{i\,arg(\mathbf{B})}\max(|\mathbf{B}| - \tau, 0) \tag{10}$$
3. Compute the convergence parameter $\varrho$:
   $$\varrho = \frac{\|\hat{\mathbf{Q}}_{f_k} - \hat{\mathbf{L}}^{i+1}_{f_k} - \hat{\mathbf{H}}^{i+1}_{f_k}\|_F}{\|\hat{\mathbf{Q}}_{f_k}\|_F}. \tag{11}$$
4. If $\varrho$ is greater than an assigned tolerance, go to point (ii), else return $\hat{\mathbf{L}}^{i+1}_{f_k}$ and $\hat{\mathbf{H}}^{i+1}_{f_k}$.

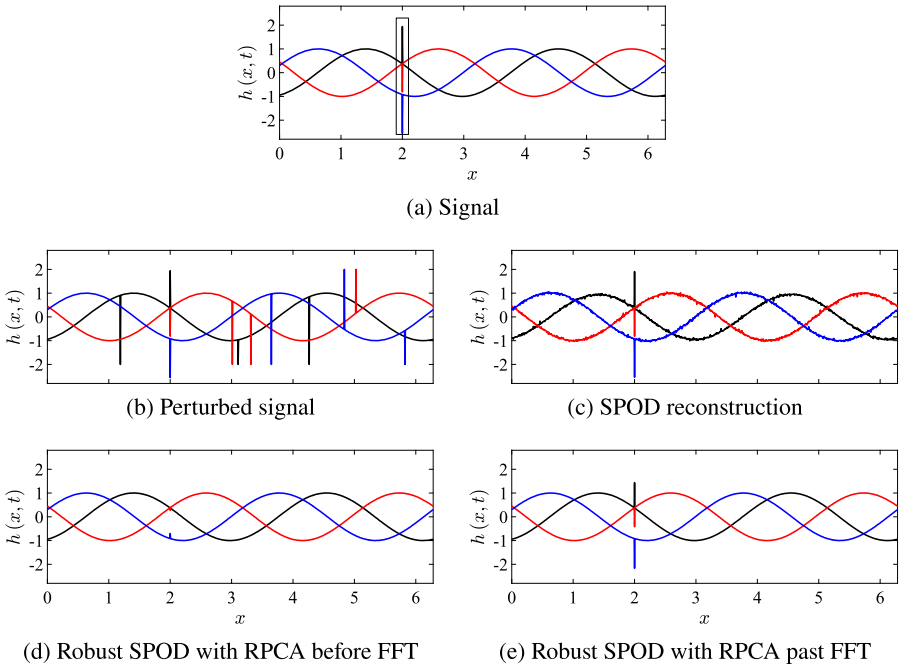


**Fig. 1.** Comparison between SPOD and robust SPOD reconstructions of a toy signal. Panel (a) reports the analyzed signal; panel (b) contains the perturbed signal with salt and pepper noise. Panel (c) reports the SPOD reconstruction by the whole spectrum of $1^{st}$ SPOD mode. Panel (d) and (e) contain the robust SPOD reconstruction with de-noising stage before and past FFT, respectively. (For interpretation of the colors in the figure(s), the reader is referred to the web version of this article.)

**Algorithm 3** Robust SPOD with principal component pursuit on each block.

1. For each data block $j = 1, ..., N_b$:
   (a) assemble data matrices
   $$\mathbf{Q}^{(j)} = \left[\boldsymbol{q}^{(j)}_{1+(j-1)(N_f-N_o)}, \boldsymbol{q}^{(j)}_{2+(j-1)(N_f-N_o)}, ..., \boldsymbol{q}^{(j)}_{N_f+(j-1)(N_f-N_o)}\right].$$
   (b) Split $\mathbf{Q}^{(j)}$ in $\mathbf{L}^{(j)}$ and $\mathbf{H}^{(j)}$ with RPCA algorithm (see Algorithm 2). Store $\mathbf{H}^{(j)}$ if needed.
   (c) Within each block perform weighted FFT
   $$\hat{\mathbf{Q}}^{(j)} = \mathcal{F}\left\{\mathbf{L}^{(j)}\boldsymbol{W}_T\right\},$$
   where $\boldsymbol{W}_T$ is the matrix of the window weights. Columns of $\hat{\mathbf{Q}}^{(j)}$, $\hat{\boldsymbol{q}}^{(j)}_k$ are the $j_{th}$ realizations of the Fourier mode at the $k^{th}$ discrete frequency $f_k$.
2. For each frequency $f_k$, with $k = 1, ..., N_f$:
   (a) Collect Fourier transform realizations in the matrices $\hat{\mathbf{Q}}_{f_k} = \sqrt{\kappa}\left[\hat{\boldsymbol{q}}^{(1)}_k, \hat{\boldsymbol{q}}^{(2)}_k, ..., \hat{\boldsymbol{q}}^{(N_b)}_k\right]$, where $\kappa = \Delta t/(N_b\|\boldsymbol{W}_T\|^2_F)$.
   (b) Calculate
   $$\mathbf{M}_{f_k} = \hat{\mathbf{Q}}^*_{f_k}\mathbf{W}\hat{\mathbf{Q}}_{f_k}.$$
   (c) Perform the eigendecomposition of $\mathbf{M}_{f_k}$
   $$\mathbf{M}_{f_k} = \boldsymbol{\Theta}_{f_k}\boldsymbol{\Lambda}_{f_k}\boldsymbol{\Theta}^*_{f_k}.$$
   For the $k^{th}$ frequency, store de-noised SPOD eigenvalues $\boldsymbol{\Lambda}_{f_k}$.
   (d) Compute de-noised SPOD modes for the $k^{th}$ frequency with
   $$\boldsymbol{\Phi}_{f_k} = \hat{\mathbf{L}}_{f_k}\boldsymbol{\Theta}_{f_k}\boldsymbol{\Lambda}^{-1/2}_{f_k}$$
3. Return $\boldsymbol{\Phi}_{f_k}$ and $\boldsymbol{\Lambda}_{f_k}$.

### 2.4. Algorithms differences

To elucidate the differences between the latter two approaches, a toy signal denoted as $h(x,t) = \cos(x - \omega t)$, with the angular frequency $\omega = 2\pi f$ and the frequency $f = 1$, has been hereafter considered. The original signal has been reported in panel (a) of Fig. 1 for different time instances with a phase delay of 45° (the temporal order of the reported curves is black, red, and blue); in $x = 2$ the signal has been set to the value $\cos(2\omega t)$ and a black rectangle highlights its location. Perturbing the signal with a salt and pepper noise (panel (b)) obtained summing to the 0.2% of corrupted data points a value equal to $\pm 2$ at each time step; one can appreciate the differences in the local dynamics. Despite this low perturbation level, the SPOD reconstruction (panel (c)) based on the entire first mode already appears particularly noisy. Panels (d) and (e) report the robust SPOD application considering the de-noising phase before and after the FFT application. As expected, the local dynamics introduced in $x = 2$ has been completely removed in panel (d).

If one is not interested in preserving local sparse dynamics, Algorithm 3 is preferred. In the following sections, the latter is employed for real-world data, the turbulent jet and the open cavity flow. In appendix A, a further comparison of the two introduced algorithms application onto the turbulent jet data is reported.

## 3. Examples

### 3.1. Turbulent jet

The first application considered in this work regards a turbulent jet presented by Schmidt et al. [34]. The jet was numerically simulated through the unstructured flow solver "Charles" [3] at a subsonic Mach number (defined as the ratio between the mean inlet jet velocity $U_j$ and the speed of sound $a_j$) equal to $M = 0.4$ and Reynolds number ($Re = U_j D_j/\nu$, with $D_j$ the nozzle diameter and $\nu$ the kinematic viscosity) of $Re = 450000$; the large-eddy computations include also the nozzle geometry where synthetic turbulence combined with a wall model is applied to obtain a fully turbulent boundary layer. The data were interpolated onto a structured cylindrical grid of $[0, 30] \times [0, 6] \times [0, 2\pi]$, respectively, in the axial ($x$), the radial ($r$) and the azimuthal ($\theta$) directions.

The analysis considers the pressure field $p$, which is decomposed in

$$p(x, r, \theta, t) = \bar{p}(x, r, \theta) + p'(x, r, \theta, t), \tag{12}$$

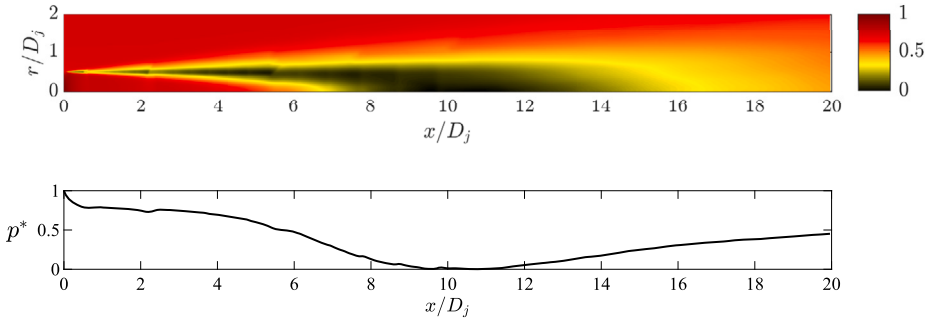


**Fig. 2.** Mean pressure distribution in the turbulent jet. Top panel depicts the temporal mean of the $m = 0$ pressure component ($\bar{p}_0$), normalized as $p^* = (\bar{p}_0 - \bar{p}_{\min})/(\bar{p}_{\max} - \bar{p}_{\min})$. The bottom panel shows the normalized mean pressure $\bar{p}_0$ variation along the jet's axis. (■■■ black, yellow, red, $0 < p^* < 1$).

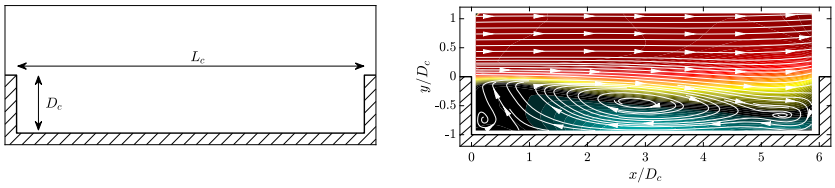


**Fig. 3.** Open cavity flows. Panel (a): geometrical sketch; panel (b): mean streamwise velocity component and streamlines distribution. Data courtesy of Zhang et al. [48]. (■■■■■ blue, cyan, black, yellow, red, $-1 < \bar{u}/\|\bar{u}\|_\infty < 1$).

where $\bar{(\cdot)}$ is the long time mean and $(\cdot)'$ represents the fluctuating part. Moreover, $p'$ is further decomposed in azimuthal Fourier modes

$$p'(x,r,\theta,t) = \sum_m \hat{p}_m(x,r,t)\mathrm{e}^{\mathrm{i}m\theta}, \tag{13}$$

$m$ being the azimuthal wavenumber. The top panel of Fig. 2 presents the spatial distribution of the mean pressure $\bar{p}_0$ ($m = 0$ Fourier component) within the turbulent jet, whereas the bottom panel reports the normalized pressure profile along the jet axis. The terms $\bar{p}_{\max}$ and $\bar{p}_{\min}$ represent the maximum and the minimum of $\bar{p}_0$, respectively. The pressure is almost constant in the potential core region ($0 < x/D_j < 5$); then it decreases in the developing jet region and finally starts to increase near the beginning of the self-similar region ($5 < x/D_j < 25$).

The present analysis is carried out considering only the $m = 0$ Fourier component; at each time instance $t_i$ the state vector $\boldsymbol{q}$ contains the evaluation of $\hat{p}_0$ in each point of the domain $(x, r)$.

### 3.2. Open cavity flow

The second investigation concerns the flow field within an open cavity, whose measurements have been acquired employing a time-resolved PIV technique. The standard SPOD tends to produce noisy outcomes, especially for non-leading modes. As demonstrated later in this paper, the application of robust SPOD enhances these modes' smoothness and physical interpretability. The data-set reported in [48] has been considered here limited to a free stream Mach number (defined as the ratio between the incoming flow velocity $U_c$ and the speed of sound $a_c$) equal to $M = 0.6$.

Panel (a) of Fig. 3 reports a sketch of the rectangular cavity. It has a length of $L_c = 158.8$ mm, a depth of $D_c = 26.4$ mm, and a width of $W_c = 101.6$ mm; the resulting nondimensional ratios are $L_c/D_c = 6$ and $W_c/D_c = 3.85$.

As depicted in panel (b) of Fig. 3, which illustrates the temporal mean distribution of the streamwise velocity component, the incoming boundary layer separates at the leading edge of the cavity, forming a shear layer. This shear layer is convectively unstable, leading to the generation of Kelvin-Helmholtz instability waves. These waves travel downstream, impinge on the back edge of the cavity, and partially reflect as acoustic waves. Then, they propagate upstream and lock-in with the Kelvin-Helmholtz instability at the leading edge, completing a feedback cycle [48,40,39]. This feedback process results in an aeroacoustic resonance whose main tones are known as Rossiter modes [31]. The characteristic dimensionless frequencies (in terms of the Strouhal number, $St$) associated with these modes can be predicted using the empirical relation from [16]:

$$St_n = \frac{f_n L_c}{U_\infty} = \frac{n - a}{1/\kappa_r + M/\sqrt{1 + (\gamma - 1)M^2/2}}. \tag{14}$$

Here, $U_\infty$ represents the freestream velocity, $\kappa_r = 0.65$ is an empirical coefficient, $a = 0.38$ is the phase lag, and $n = 1, 2, \ldots$ corresponds to the Rossiter mode index. Equation (14) predicts the dimensionless frequencies $St_n$ associated with the resonance modes in open cavities.

## 4. Application to fluid flows

### 4.1. Turbulent jet

The standard SPOD algorithm is initially used to determine the principal frequencies of the turbulent jet, also reporting the main coherent structures of the $1^{st}$ and $2^{nd}$ mode; later, the data is artificially corrupted by comparing the performance of the SPOD and robust SPOD procedures separately.

The snapshots have been sampled with a dimensionless time equal to 0.2, and a total of $N_t = 10000$ snapshots were considered. For the SPOD analysis, $N_f = 128$ snapshots have been used, considering a Hamming temporal window and a 50% overlap among blocks. This resulted in $N_b = 155$ blocks. It's worth noting that in this particular test, where only the $\hat{p}_0$ component was considered, the spatial weights were determined by considering only the integration quadrature, following the approach outlined by Schmidt and Colonius [36]. Fig. 4 displays the SPOD spectrum as a function of the Strouhal number $St = f D_j/U_j$. The most prominent modal separation is observed at $St \approx 0.4$. Fig. 5 exhibits the real part of the first two SPOD modes at different values of the Strouhal number. The pressure field forms a compact wavepacket in the initial shear-layer region of the jet, similar to a Kelvin–Helmholtz shear-layer instability as shown by Schmidt et al. [34].

To assess the robustness of the SPOD method, artificial data corruption was introduced by randomly selecting a certain percentage of

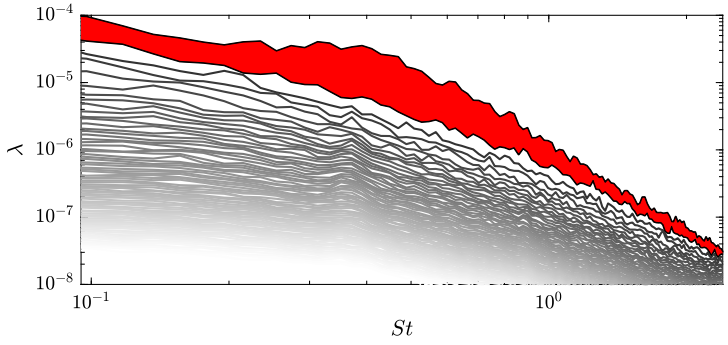


**Fig. 4.** SPOD spectrum for the turbulent jet. The red-shaded area highlights the separation between the first and the second mode.

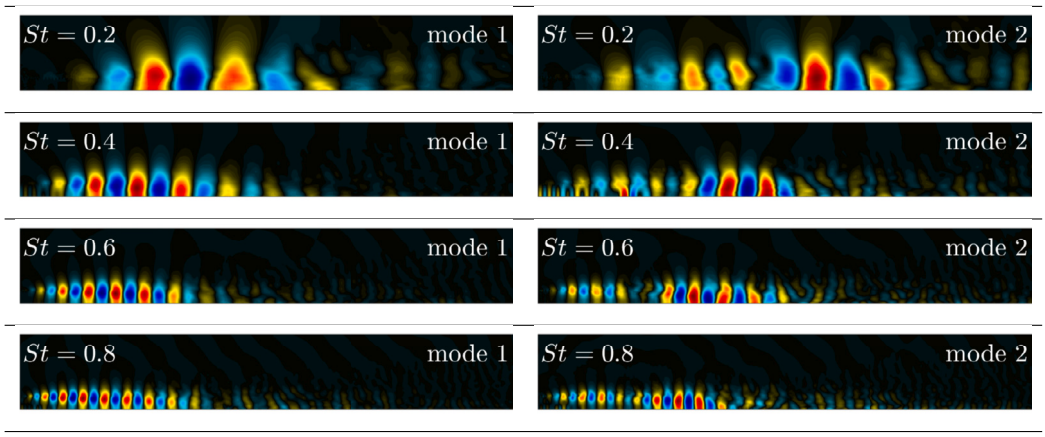


**Fig. 5.** Real part of $1^{st}$ and $2^{nd}$ mode at different $St$. Modes have been normalized with respect to their maximum. In all the panels, the abscissa and ordinate are the dimensionless axial coordinate $x/D_j$ and radial coordinate $r/D_j$, respectively, omitted for clarity. ($0 < x/D_j < 20$ and $0 < r/D_j < 3$, blue, cyan, black, yellow, red, $-1 < \phi_{f_k}/\|\phi_{f_k}\|_\infty < 1$).

corrupted data points across the spatial domain at each time step. The pressure field hereafter represented is limited to the shear layer region only, $x/D_j < 4$, with a grid of $n_x \times n_y = 137 \times 45 = 6115$ points. Note that the robust SPOD algorithm was unaware of the specific locations of these corrupted data points. Two kinds of data corruption have been considered:

- Gaussian noise with zero mean and $4p_{\max}$ variance, $p_{\max}$ being the maximum of the $\hat{p}_0$ component;
- Salt and pepper noise with values of $\pm 4p_{\max}$.

These noises introduce a high perturbation in the $L_2$ norm of the flow even with a low percentage of corrupted data points. It is important to note that if salt and pepper noise is added to the entire 3D distribution, the averaging process inherent in computing the $m = 0$ mode would alter the noise characteristics. The resulting noise will no longer have the distinct characteristics of salt and pepper noise. Instead, it would resemble a Gaussian-like distribution due to the central limit theorem.

The differences between the two techniques are highlighted in Fig. 6 which reports a comparison between the coherent structures of the $1^{st}$ mode at different $St$ values, computed with the SPOD and robust SPOD technique; the results refer to the salt and pepper corruption of the 10% of the data and consider different values of $\alpha$, defined in Eq. (8). Panels in the first line contain the real part of the leading SPOD mode at $St =$ 0.4, 0.8, and 1.2, considering the corrupted data; they show how a quite small percentage of corrupted data results in noisy modes, particularly at higher frequencies. The use of robust SPOD relevantly improves the modes' quality; the influence of the $\alpha$ parameter, as discussed in [33], can be observed regarding noise filtering. The higher the $\alpha$, the lower the filtering effects. The value $\alpha = 2$ gives the modes corresponding to the uncorrupted configuration (not shown herein); see [34].

The effectiveness of the robust SPOD technique is also confirmed with Gaussian noise. Indeed, Fig. 7 clearly shows how the robust SPOD algorithm enhances the modes' quality and accuracy.

To quantify the validity of the robust SPOD, the relative error, denoted as $\varepsilon_{fk}$, is introduced as:

$$\varepsilon_{fk} = \frac{\|\boldsymbol{\phi}_{f_k}^{corr} - \boldsymbol{\phi}_{f_k}\|_2}{\|\boldsymbol{\phi}_{f_k}\|_2}, \tag{15}$$

in which $\boldsymbol{\phi}_{f_k}$ denotes the original SPOD modes and $\boldsymbol{\phi}_{f_k}^{corr}$ refers to the modes obtained from corrupted data using either SPOD or robust SPOD. This relative error measures the accuracy and reliability of the robust SPOD technique. The dependency of $\varepsilon_{fk}$ with respect $\alpha$ and $St$ has been reported in Figs. 8 and 9, respectively. Fig. 8 refers to two different types of noise, various percentages of corrupted data points, and different values of $\alpha$, specifically at the leading frequency $St = 0.4$. Solid lines in both panels represent the $\varepsilon_{f_k}$ at several $\alpha$, color-coded according to the percentage of corrupted data points. The dashed lines represent the SPOD error, specifically when $\alpha$ approaches infinity. Each curve exhibits its unique minimum for $\alpha$, but regardless of the error type or the percentage of corrupted data points, as in [33], the lowest values of $\varepsilon_{fk}$ are found when $\alpha$ is O(1), approximately in the range of $1 \sim 3$. Fig. 9, instead, reports the results for the salt and pepper noise only, highlighting the influence of the de-noising parameter $\alpha$ on the mode error $\varepsilon$ for the first four modes as a function of $St$. The effect of the de-noising parameter $\alpha$ on the mode error varies with the frequency of interest; the relative performance of robust SPOD tends to be more pronounced and

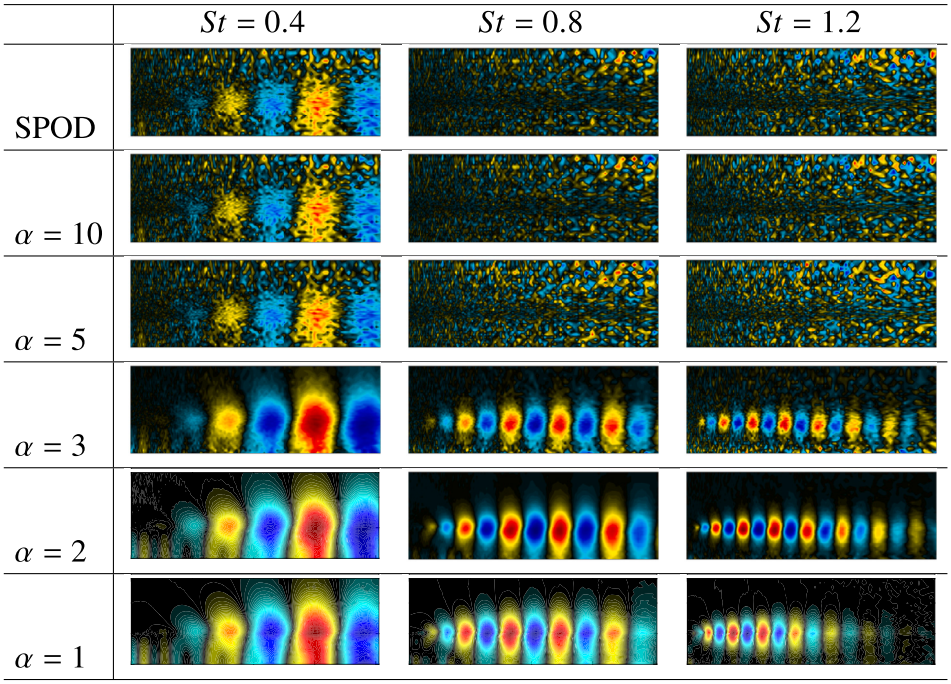


**Fig. 6.** Comparison between SPOD and robust SPOD leading modes at different $St$. Salt and pepper noise with the 10% of corrupted data points. Panels in the first line refer to SPOD. Other rows show the effect of the de-noising parameter $\alpha$ on the robust SPOD modes. Data corruption modeled as salt and pepper noise $\pm 4p_{\max}$. In all the panels, the abscissa and ordinate are the dimensionless axial coordinate $x/D_j$ and radial coordinate $r/D_j$, respectively, omitted for clarity. Field variables have been normalized with respect to their maximum. ($0 < x/D_j < 4$ and $0 < r/D_j < 1.5$, blue, cyan, black, yellow, red, $-1 < \phi_{f_k}/\|\phi_{f_k}\|_\infty < 1$).

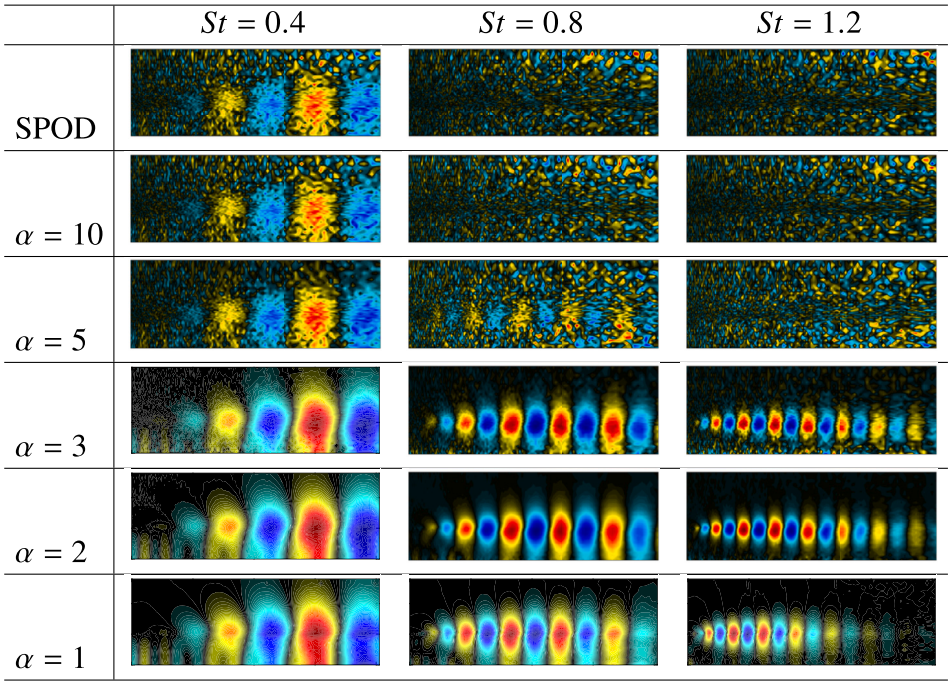


**Fig. 7.** Comparison between SPOD and robust SPOD leading modes at different $St$. Gaussian noise with the 10% of corrupted data points. Panels in the first line refer to SPOD modes of corrupted data. Other rows show the effect of the de-noising parameter $\alpha$ on the robust SPOD modes. Data corruption is modeled as Gaussian noise with $\pm 4p_{\max}$ variance. In all the panels, the abscissa and ordinate are the dimensionless axial coordinate $x/D_j$ and radial coordinate $r/D_j$, respectively, omitted for clarity. Field variables have been normalized with respect to their maximum. ($0 < x/D_j < 4$ and $0 < r/D_j < 1.5$, blue, cyan, black, yellow, red, $-1 < \phi_{f_k}/\|\phi_{f_k}\|_\infty < 1$).

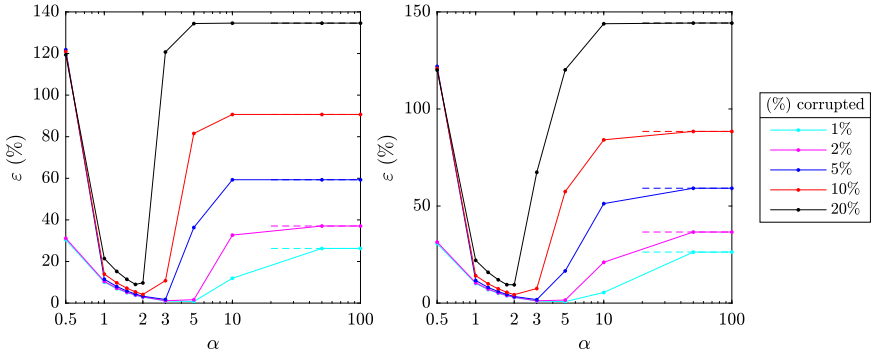


(a) Salt and pepper noise (b) Gaussian noise

**Fig. 8.** Relative error $\varepsilon$ at $St = 0.4$ computed with SPOD and robust SPOD techniques for different levels and types of noise, considering several values of $\alpha$. Solid lines represent the $\varepsilon$ at several $\alpha$, color-coded according to the corrupted data points percentage. Dashed lines represent the SPOD error, namely $\alpha$ approaching infinity.

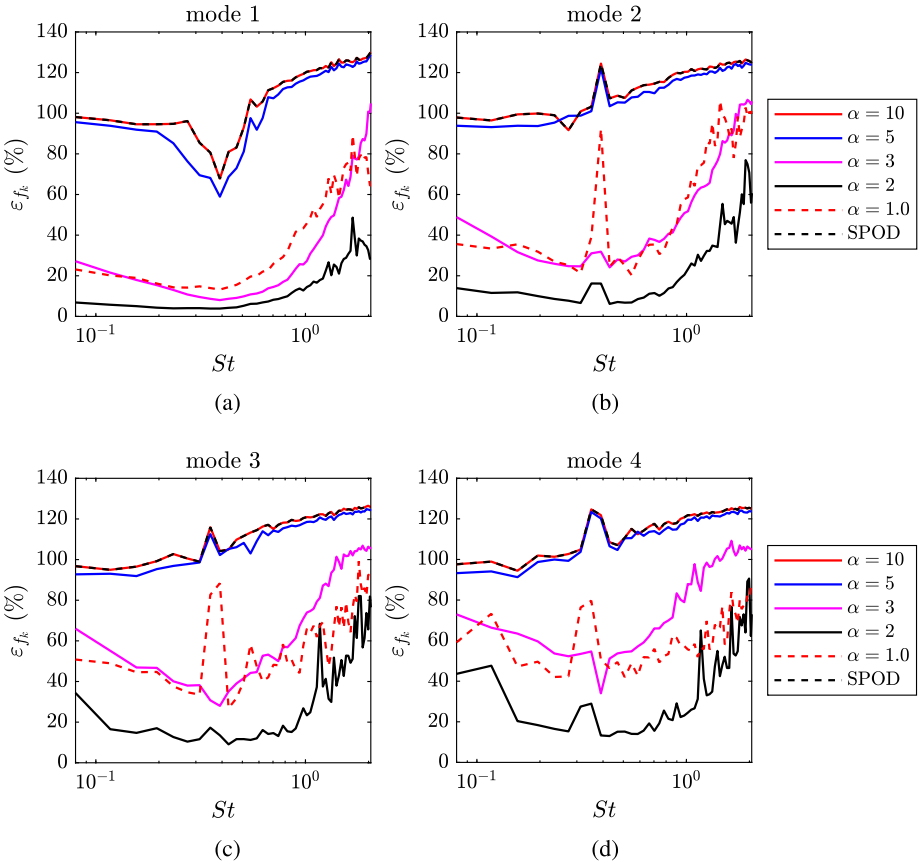


(a) (b) (c) (d)

**Fig. 9.** Effect of de-noising parameter $\alpha$ on the error $\varepsilon_{f_k}$. Panels (a) to (d) go from the $1^{st}$ to the $4^{th}$ SPOD mode. Salt and pepper noise with 10% of corrupted data points.

advantageous at higher $St$ values. For this case, the optimal choice of $\alpha$ is 2.

The SPOD spectrum is strongly affected by $\alpha$. Fig. 10 reports both the SPOD spectra of the clean (red lines) and corrupted (dashed magenta curves) configurations and those obtained by the robust SPOD at various filter levels (black curves). Even in a limited number of data points, the introduction of noise significantly perturbs the spectrum. At high $\alpha$ values, the robust SPOD produces precisely the same spectrum of the SPOD technique; a reduction of $\alpha$ is accompanied by a decrease in the noise levels and, thus, the robust spectrum tends towards the clean one (the optimum is at $\alpha = 2$). This optimal value balances noise reduction and preservation of relevant flow features.

Finally, robust SPOD can also be a valuable tool for de-noising data and reconstructing the signal from de-noised modes. This ability is reported in Fig. 11, which contains a snapshot of the original pressure fluctuation (left panel, first row), the corresponding perturbed field (central panel, first row) considering the 10% of corrupted data points, the SPOD reconstruction (right panel, first row) and various robust SPOD reconstructions (panels in the second row). Based on the entire spectrum of the first three modes, the SPOD reconstruction shows noticeable noise levels. Lower panels demonstrate the de-noising effect achieved by adjusting the parameter $\alpha$, which increases as $\alpha$ reduces. For values lower than 5, the reconstructed snapshots exhibit a remarkable noise reduction, leading to a clearer representation of the underlying flow structures.

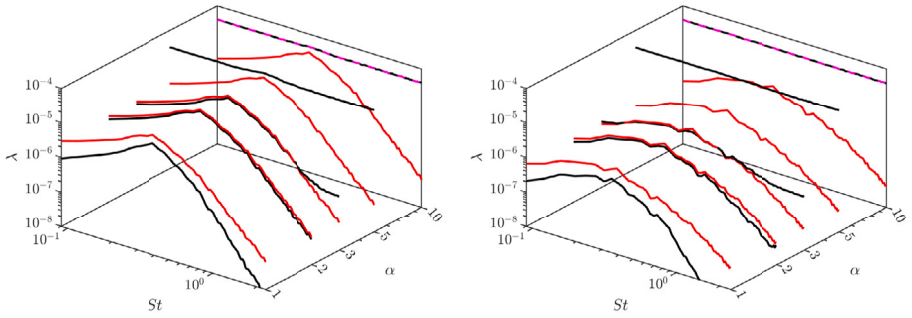


**Fig. 10.** Effect of de-noising parameter $\alpha$ on the robust SPOD spectrum. Panel (a) refers to $1^{st}$ SPOD mode, and panel (b) to the $2^{nd}$ one. Black lines represent the robust SPOD spectra, and red lines the original SPOD spectrum. Dashed magenta lines are the SPOD spectra of corrupted data. Salt and pepper noise with 10% of corrupted data points.

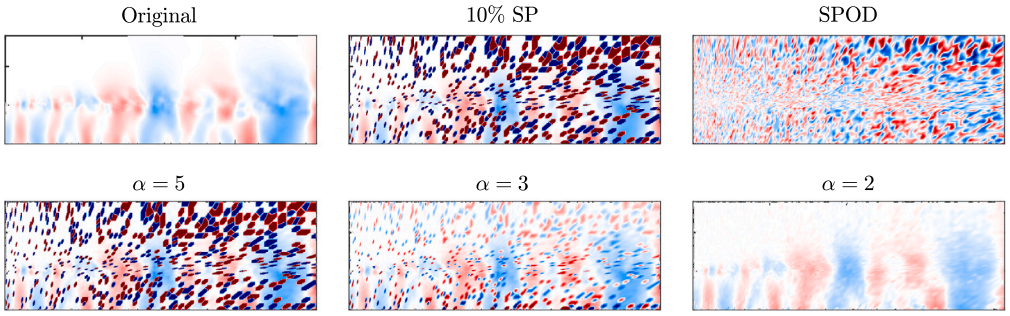


**Fig. 11.** De-noising with robust SPOD. The left panel, first row, contains a $\hat{p}_0$ sample snapshot. The central panel, first row, shows the 10% of corrupted data points with salt and pepper noise. The right panel, first row, reports an attempt at de-noising with SPOD by employing the spectrum of the first three modes. Panels in the second row represent the robust SPOD reconstruction by employing the spectrum of all the robust SPOD modes, highlighting the de-noising effect of the parameter $\alpha$. ($0 < x/D_j < 4$ and $0 < r/D_j < 1.5$).

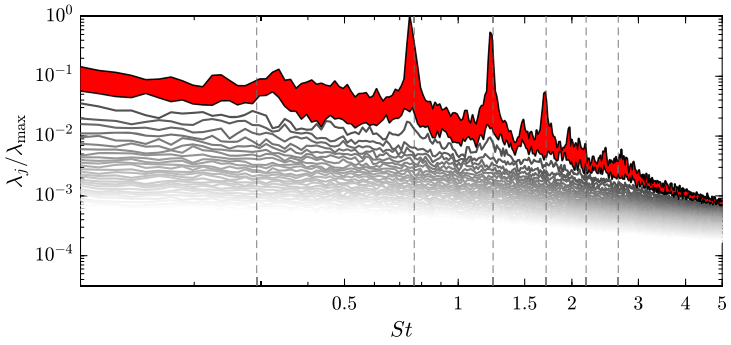


**Fig. 12.** SPOD spectrum of open cavity flows from [48]. Case with $M = 0.6$. Vertical dashed lines represent Rossiter frequencies from Eq. (14). The red shaded area highlights the separation between the first and the second mode.

### 4.2. Open cavity flow

The open flow cavity data-set consists of TR-PIV data by Zhang et al. [48]. Velocity components were measured on a uniform grid with dimensions $n_x \times n_y = 156 \times 55$ and with a sampling frequency of $f_s = 16000$ Hz. The analysis is based on $N_t = 16000$ snapshots, with $N_b = 30$ blocks and $N_f = 1024$ frequencies. The corresponding spectrum has been reported in Fig. 12; a good agreement between the leading frequencies and the Rossiter frequencies, predicted by Eq. (14) and indicated by vertical dashed lines, can be appreciated.

Fig. 13 presents the real part of the first SPOD mode at the two leading frequencies, $St = 0.75$ and $St = 1.22$. Panels (a) and (b) show the streamwise component of the mode, while panels (c) and (d) report the transversal component. The spatial structures at higher frequencies exhibit finer scales than those at lower frequencies. Panels (d) and (e), instead, contain the magnitude of velocity mode gradients, defined as the square root of the sum of squares of the individual velocity mode gradient components:

$$\xi_{f_k}(x,y) = \sqrt{\left(\frac{\partial \phi_{u_{f_k}}}{\partial x}\right)^2 + \left(\frac{\partial \phi_{u_{f_k}}}{\partial y}\right)^2 + \left(\frac{\partial \phi_{v_{f_k}}}{\partial x}\right)^2 + \left(\frac{\partial \phi_{v_{f_k}}}{\partial y}\right)^2}. \quad (16)$$

It provides crucial information about the spatial distribution and intensity of flow structures within the open cavity. This field variable will provide valuable insights for analyzing modes smoothness that will be carried out hereafter.

For this case, the robust SPOD analysis is based on the Algorithm 3, with a de-noising parameter $\alpha = 1$. Fig. 14 presents the spectra obtained from both SPOD (red lines) and robust SPOD (black lines) analysis. The robust SPOD analysis primarily focuses on reducing noise at high frequencies, meaning that the obtained reconstructed signals exhibit less

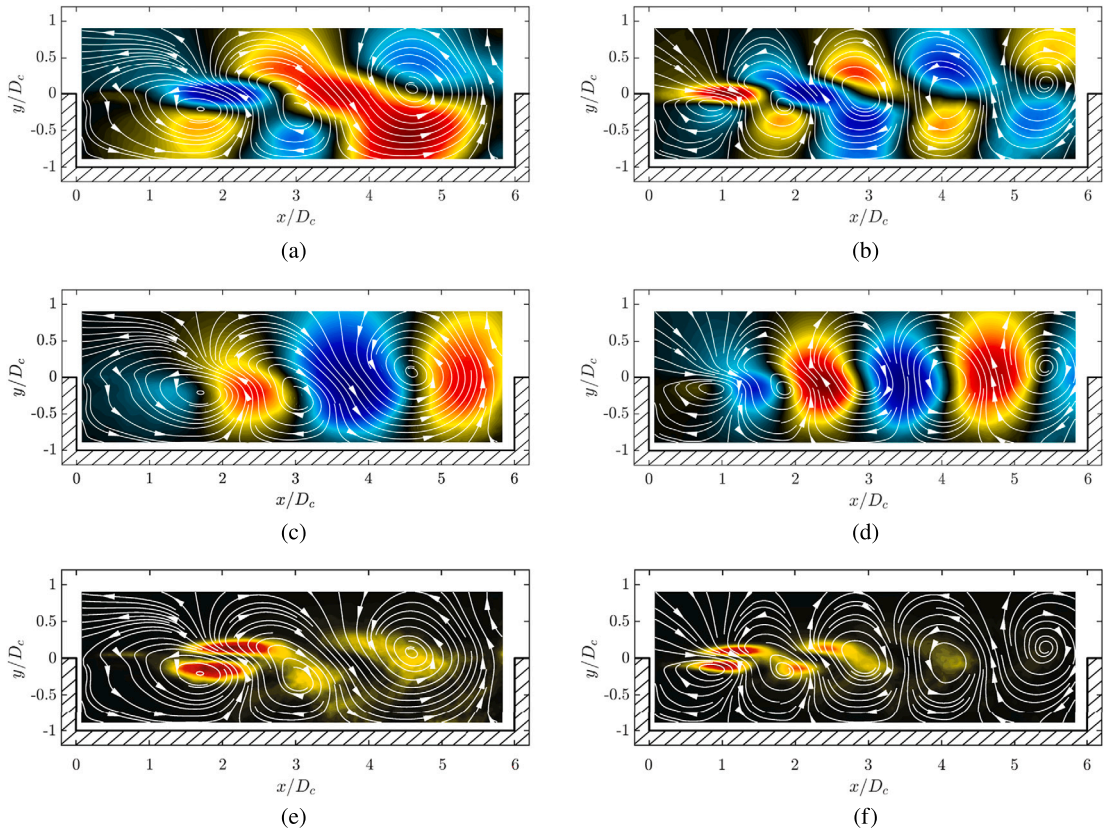


**Fig. 13.** Leading SPOD modes of open cavity flows data from Zhang et al. [48]. Panel (a): real part of leading SPOD mode of $u$ at $St = 0.75$. Panel (b): real part of leading SPOD mode of $u$ at $St = 1.22$. Panel (c): real part of leading SPOD mode of $v$ at $St = 0.75$. Panel (d): real part of leading SPOD mode of $v$ at $St = 1.22$. Panel (e): magnitude of velocity mode gradient $m_{f_k}$ at $St = 0.75$. Panel (f): magnitude of velocity mode gradient $\xi_{f_k}$ at $St = 0.75$. White lines are the streamlines pattern viewed by an observer moving with the mean flow. Field variables have been normalized with respect to their maximum.

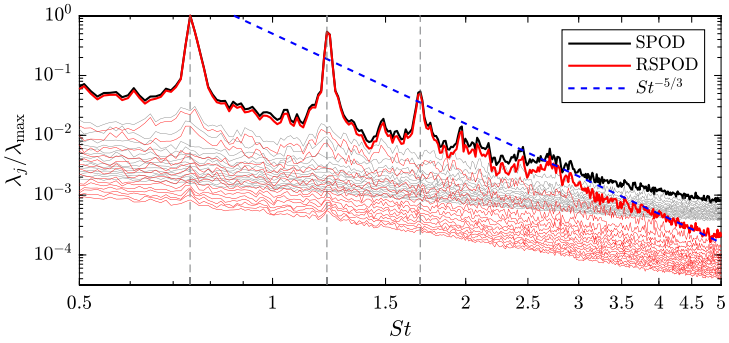


**Fig. 14.** Comparison between the SPOD spectrum (black) and the robust SPOD one (red) for the cavity flow. The reference blue dashed curve represents $St^{-5/3}$. Vertical dashed lines represent Rossiter frequencies. Note that for robust SPOD the Algorithm 3 has been employed.

noise contamination than those obtained from SPOD, particularly in the higher frequency range. To provide a reference for the spectral behavior, the blue dashed line represents the Kolmogorov power law ($St^{-5/3}$), which is a well-established representation of the energy spectrum in turbulent flows and serves as a benchmark for assessing the spectral characteristics of the analyzed data [46,18,30], showing how the curve tends to align with this well-known benchmark. As expected, the power law scaling is not valid at low frequencies, where relatively larger coherent structures characterize the flow.

Figs. 15 and 16 compare the leading $u$ and $v$ modes, respectively, obtained from both SPOD and robust SPOD analysis. The comparison is done for the first four Rossiter frequencies and a generic high Strouhal number ($St = 4$).

It is worth noting that applying robust SPOD leads to considerable improvements in the smoothness of the extracted modes. Specifically, SPOD already performs well for the first mode at the leading frequencies ($St = 0.75$ and $St = 1.70$), producing relatively smooth modes. However, for the remaining modes, the employment of robust SPOD significantly enhances the smoothness of the modes. Moreover, at high frequencies, such as $St = 4$, the coherent structures extracted with the SPOD technique are not easily recognizable, whereas the robust SPOD modes exhibit clearer and more distinguishable coherent structures. The structures extracted with RSPOD are in accordance with literature studies [39,24,37,20,22].

To quantify the roughness of the modes, following [13], it is convenient to compute the spatial standard deviation of the velocity mode gradient magnitude defined in Eq. (16):

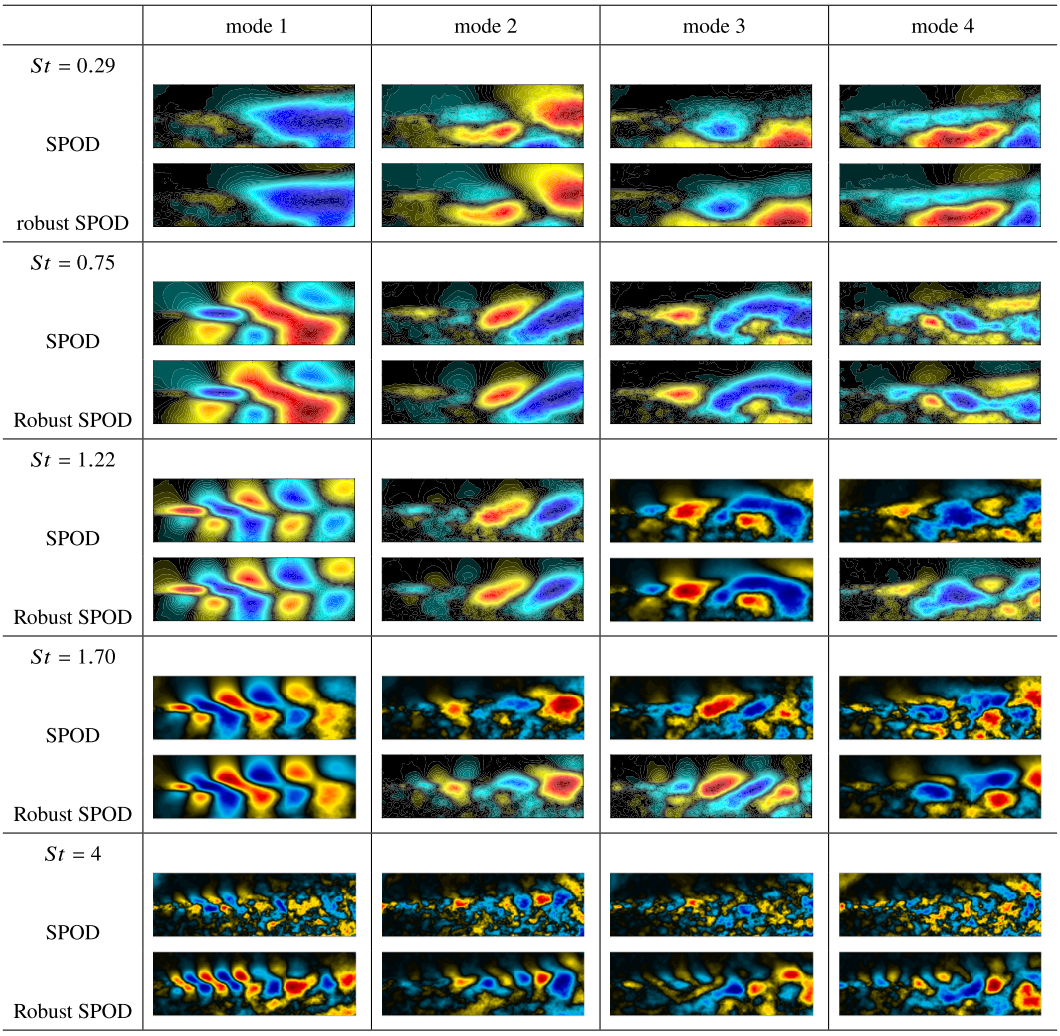


**Fig. 15.** Comparison between SPOD and robust SPOD leading $u$ modes at different $St$. Field variables have been normalized with respect to their maximum. Note that for robust SPOD the Algorithm 3 has been employed. De-noising parameter $\alpha = 1$. In all the panels, the abscissa and ordinate are the dimensionless axial coordinate $x/D_c$ and radial coordinate $r/D_c$, respectively, omitted for clarity. (■■■■■ blue, cyan, black, yellow, red, $-1 < \phi_{f_k}/\|\phi_{f_k}\|_\infty < 1$).

$$\sigma_{f_k} = \mathrm{std}(\xi_{f_k}) = \sqrt{\frac{1}{n_x n_y}\sum_{i=1}^{n_x}\sum_{j=1}^{n_y}\left(\xi_{f_k}(x_i, y_j) - \bar{\xi}_{f_k}\right)^2} \tag{17}$$

where $\bar{\xi}_{f_k} = \frac{1}{n_x n_y}\sum_{i=1}^{n_x}\sum_{j=1}^{n_y}\xi_{f_k}(x_i, y_j)$. Fig. 17 displays the $\sigma_{f_k}$ values for the leading four modes obtained from both SPOD and robust SPOD analysis. Comparing the two sets of modes, it is evident that the robust SPOD modes exhibit greater smoothness, particularly at high Strouhal numbers ($St$). The lower values of $\sigma_{f_k}$ for robust SPOD modes indicate reduced roughness and enhanced coherence in flow field structures.

## 5. Discussion and conclusions

This work represents a step forward in analyzing experimental measurements, where corrupted data and outliers can influence the extraction of coherent structures using traditional modal analysis techniques. This process is much more challenging at higher frequencies, where noise and uncertainties seriously affect data integrity.

A novel approach overcomes these limitations, the robust spectral proper orthogonal decomposition, here introduced, incorporating the robust principal component analysis within the SPOD algorithm. The investigation focused on evaluating the potential of this innovative method in improving the extraction of coherent structures from complex data-sets. The effectiveness of robust SPOD was properly tested through two distinct fluid dynamics problems: the subsonic jet, investigated through numerical simulations, and the flow within an open cavity, analyzed through experimental measurements.

This work presents two alternative algorithms: one removes sparse noise on the realizations of Fourier modes, while the other does it directly on the snapshot blocks. The first approach preserves possible sparse local dynamics of the flow, while the second is preferred when prioritizing the smoothness of the modes over such preservation. It's important to note that robust PCA performs better when a high number of snapshots are considered for this stage. This implies that given the number of snapshots available for analysis and once the optimal number of frequencies has been chosen along with the blocks overlap and subsequently the number of blocks, if the number of blocks greatly exceeds the number of snapshots per block, one should prefer Algorithm 1, while if the opposite holds true, Algorithm 3 is preferable.

A crucial parameter for robust SPOD, in both algorithms, is the de-noising parameter $\alpha$. In this work, it has been highlighted that the best practice for choosing $\alpha$ falls within the interval of $1 \sim 3$, confirming the literature's results suggesting that the optimal $\alpha$ is of order 1.

Robust SPOD demonstrates superior performance by providing effectively converged and physically interpretable modes compared to those of classical SPOD, especially at high frequencies. The new technique has been proved a powerful tool for data de-noising as well; indeed, by reconstructing signals from de-noised modes, it was demonstrated that

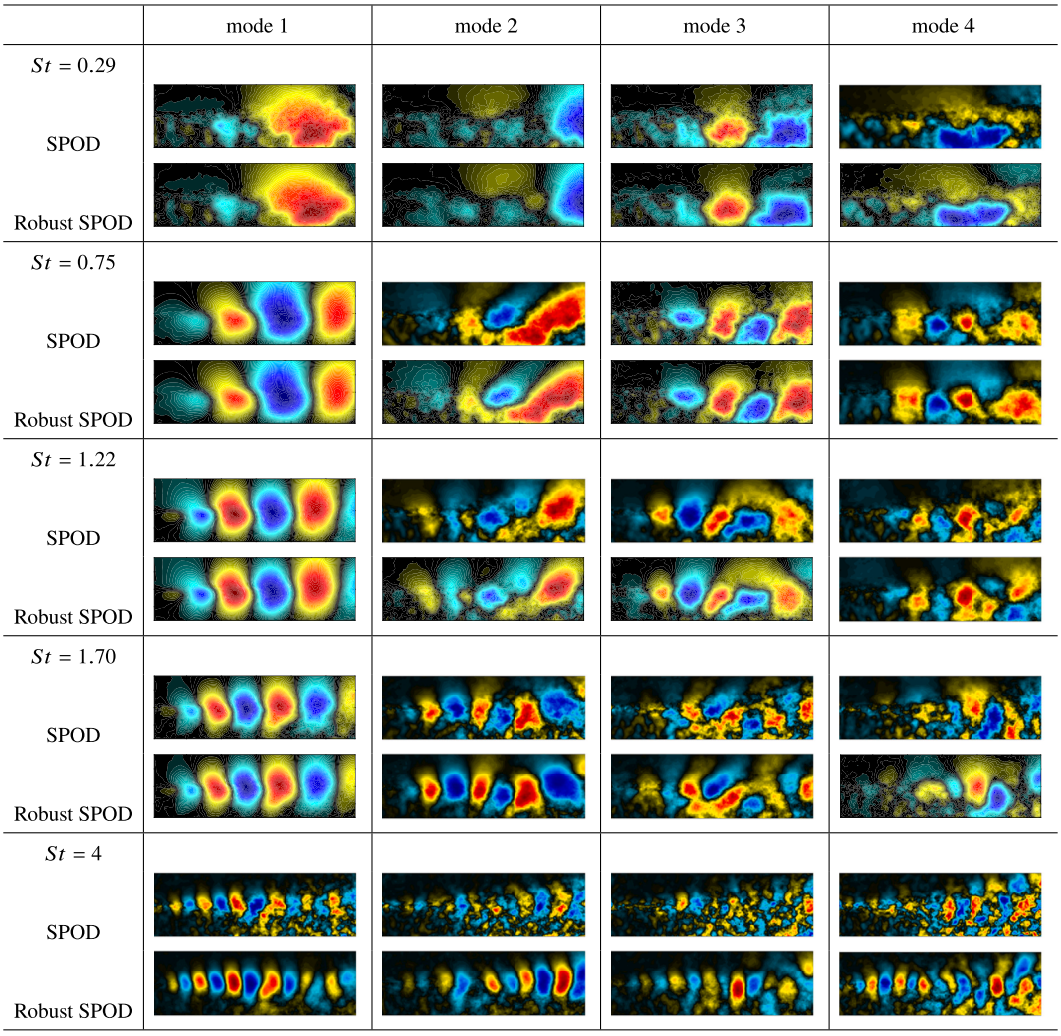


**Fig. 16.** Comparison between SPOD and robust SPOD leading $v$ modes at different $St$. Field variables have been normalized with respect to their maximum. Note that for robust SPOD the Algorithm 3 has been employed. De-noising parameter $\alpha = 1$. In all the panels, the abscissa and ordinate are the dimensionless axial coordinate $x/D_c$ and radial coordinate $r/D_c$, respectively, omitted for clarity. (■■■■■ blue, cyan, black, yellow, red, $-1 < \phi_{f_k}/\|\phi_{f_k}\|_\infty < 1$).

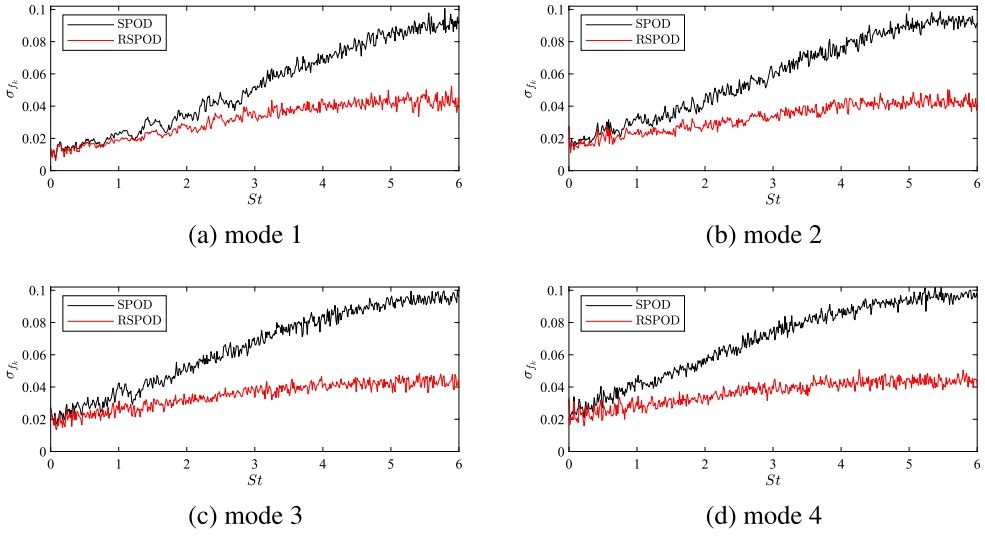


**Fig. 17.** Spatial standard deviation of the velocity mode gradient magnitude. Comparison between SPOD and robust SPOD.

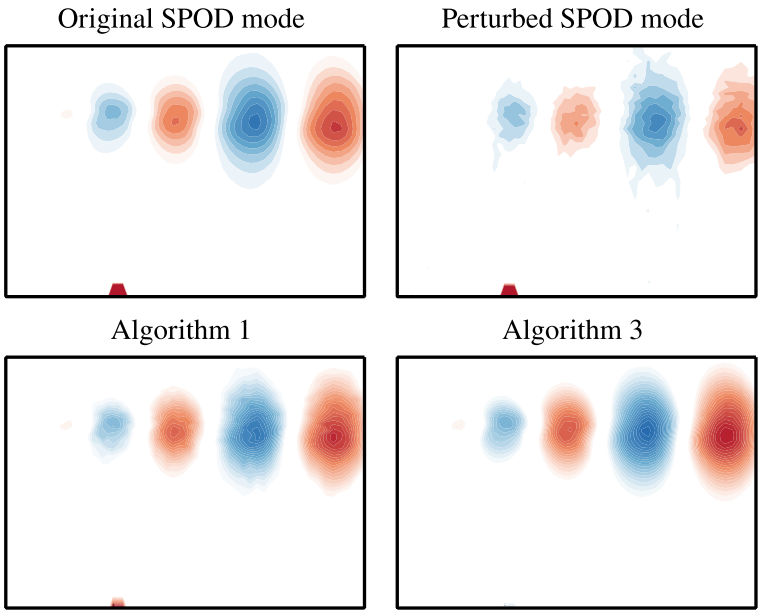


**Fig. A.18.** Comparison between robust SPOD algorithms using the turbulent jet data with a synthetic cosine signal at $x/D_j = 0.3$. Salt and pepper noise with the 0.2% of corrupted data points has been considered. In all the panels, the abscissa and ordinate are the dimensionless axial coordinate $x/D_j$ $(0 < x/D_j < 1)$ and radial coordinate $r/D_j$ $(0 < r/D_j < 0.7)$, respectively, omitted for clarity. The left panel, first row, shows the leading SPOD mode at $St = 1.2$ near the inlet section. The right panel, first row, displays the same SPOD mode obtained from the corrupt data-set. Panels in the second row illustrate the application of the two robust SPOD algorithms with the same denoising parameter $\alpha = 2$. Field variables have been normalized with respect to their maximum. (■ ■ blue, white, red, $-1 < \phi_{f_k}/\|\phi_{f_k}\|_\infty < 1$).

robust SPOD mitigates the detrimental effects of noise and uncertainties, facilitating the data interpretation.

In conclusion, the robust SPOD technique represents a significant advancement in the field of modal analysis, in particular for the treatment of experimental measurements. It not only addresses the challenges posed by corrupted data and outliers but also extends its utility to removing data noise and improving the reliability of results. The promising outcomes from both numerical and experimental data-set suggest that robust SPOD holds exciting potential for advancing the understanding of complex fluid dynamics phenomena and improving the robustness of modal analysis in various practical applications.

## CRediT authorship contribution statement

**Antonio Colanera:** Writing – original draft, Visualization, Validation, Methodology, Investigation, Formal analysis, Data curation, Conceptualization. **Oliver T. Schmidt:** Writing – review & editing, Validation, Supervision, Formal analysis. **Matteo Chiatto:** Writing – review & editing, Validation, Supervision, Formal analysis.

## Declaration of competing interest

The authors declare that they have no known competing financial interests or personal relationships that could have appeared to influence the work reported in this paper.

## Acknowledgements

The authors would like to acknowledge Luigi de Luca for his insightful comments and suggestions, and Louis Cattafesta for sharing experimental data on the open cavity flow.

## Appendix A. Different robust SPOD algorithms

This section compares the effects of the different robust SPOD algorithms on the turbulent jet data (analyzed in Section 4.1). At the location $x/D_j = 0.3$ along the axis $r = 0$, a synthetic cosine signal with a forcing frequency corresponding to $St = 1.2$ has been implemented. The left panel, first row, of Fig. A.18 presents a zoomed-in view near the inlet section $(0 < x/D_j < 1)$ of the leading pressure SPOD mode at $St = 1.2$. This mode exhibits the oscillating pressure pattern previously observed in the paper and captures the synthetic signal. Subsequently, salt and pepper noise is introduced to corrupt only 0.2% of the data-set. The right panel, first row, of the figure displays the same SPOD mode obtained from the corrupt data-set. While the synthetic signal remains detectable, the noise introduced by such a low number of corrupted data points results in significantly noisier modes. Panels in the second row represent the application of both robust SPOD algorithms, both with the same denoising parameter $\alpha = 2$. It is evident that Algorithm 1, while providing less smooth modes, preserves the local sparse dynamics; on the other hand, Algorithm 3 should be preferred if local behaviors are not of primary interest.

## Data availability

Data will be made available on request.

## References

[1] L.I. Abreu, A.V.G. Cavalieri, P. Schlatter, R. Vinuesa, D.S. Henningson, Spectral proper orthogonal decomposition and resolvent analysis of near-wall coherent structures in turbulent pipe flows, J. Fluid Mech. (2020), https://doi.org/10.1017/jfm.2020.445.

[2] J.S. Bendat, A.G. Piersol, Random Data: Analysis and Measurement Procedures, Wiley, 2010.

[3] G. Brès, F. Ham, J. Nichols, S. Lele, Unstructured large-eddy simulations of supersonic jets, AIAA J. 55 (2017) 1164–1184, https://doi.org/10.2514/1.J057012.

[4] M. Buzzicotti, F. Bonaccorso, P.C. Di Leoni, L. Biferale, Reconstruction of turbulent data with deep generative models for semantic inpainting from turb-rot database, Phys. Rev. Fluids 6 (2021), https://doi.org/10.1103/PhysRevFluids.6.050503.

[5] E. Candes, X. Li, Y. Ma, J. Wright, Robust principal component analysis?, J. ACM 58 (2009), https://doi.org/10.1145/1970392.1970395.

[6] M. Chiatto, C. Cardinale, J.K. Shang, F. Grasso, Analysis of the wake flow behind concave curved cylinders with velocity measurements by particle image velocimetry and modal decomposition, Phys. Fluids 35 (2023), https://doi.org/10.1063/5.0158000.

[7] M. Chiatto, L. de Luca, F. Grasso, Modal analysis of actively controlled flow past a backward facing ramp, Phys. Rev. Fluids 6 (2021) 064608, https://doi.org/10.1103/PhysRevFluids.6.064608.
[8] M. Chiatto, J.K. Shang, L. de Luca, F. Grasso, Insights into low Reynolds flow past finite curved cylinders, Phys. Fluids 33 (2021) 035150, https://doi.org/10.1063/5.0043222.
[9] S. Chu, C. Xia, H. Wang, Y. Fan, Z. Yang, Three-dimensional spectral proper orthogonal decomposition analyses of the turbulent flow around a seal-vibrissa-shaped cylinder, Phys. Fluids 33 (2021) 025106, https://doi.org/10.1063/5.0035789.
[10] A. Colanera, A. Della Pia, M. Chiatto, L. de Luca, F. Grasso, Modal decomposition analysis of unsteady viscous liquid sheet flows, Phys. Fluids 33 (2021) 092117, https://doi.org/10.1063/5.0065683.
[11] S. Discetti, Y. Liu, Machine learning for flow field measurements: a perspective, Meas. Sci. Technol. 34 (2023), https://doi.org/10.1088/1361-6501/ac9991.
[12] R.M. Everson, L. Sirovich, Karhunen–Loève procedure for gappy data, J. Opt. Soc. Am. A, Opt. Image Sci. Vis. 12 (1995) 1657–1664.
[13] C.H. Grohmann, M.J. Smith, C. Riccomini, Multiscale analysis of topographic surface roughness in the midland valley, Scotland, IEEE Trans. Geosci. Remote Sens. 49 (2011) 1200–1213, https://doi.org/10.1109/TGRS.2010.2053546.
[14] H. Gunes, S. Sirisup, G. Karniadakis, Gappy data: to krig or not to krig?, J. Comput. Phys. 212 (2006) 358–382, https://doi.org/10.1016/j.jcp.2005.06.023.
[15] X. He, Z. Fang, G. Rigas, M. Vahdati, Spectral proper orthogonal decomposition of compressor tip leakage flow, Phys. Fluids 33 (2021) 105105, https://doi.org/10.1063/5.0065929.
[16] H. Heller, D. Bliss, The physical mechanism of flow-induced pressure fluctuations in cavities and concepts for their suppression, https://doi.org/10.2514/6.1975-491, 1975.
[17] H. Huang, D. Dabiri, M. Gharib, On errors of digital particle image velocimetry, Meas. Sci. Technol. 8 (1997) 1427–1440, https://doi.org/10.1088/0957-0233/8/12/007.
[18] P. Kuhn, J. Soria, K. Oberleithner, Linear modelling of self-similar jet turbulence, J. Fluid Mech. 919 (2021), https://doi.org/10.1017/jfm.2021.292.
[19] S. Lawrence, Turbulence and the dynamics of coherent structures. I. Coherent structures, Q. Appl. Math. 45 (1987) 561–571.
[20] S. Lawson, G. Barakos, Review of numerical simulations for high-speed, turbulent cavity flows, Prog. Aerosp. Sci. 47 (2011) 186–216, https://doi.org/10.1016/j.paerosci.2010.11.002.
[21] Z. Lin, M. Chen, Y. Ma, The augmented Lagrange multiplier method for exact recovery of corrupted low-rank matrices, Math. Program. 9 (2010).
[22] H. Liu, C. Yan, Y. Zhao, Y. Qin, Analysis of pressure fluctuation in transonic cavity flows using modal decomposition, Aerosp. Sci. Technol. 77 (2018) 819–835, https://doi.org/10.1016/j.ast.2018.03.033.
[23] D. Manolakis, V. Ingle, S. Kogon, Statistical and Adaptive Signal Processing: Spectral Estimation, Signal Modeling, Adaptive Filtering and Array Processing, Artech House Signal Processing Library, 2005.
[24] N. Murray, E. Sällström, L. Ukeiley, Properties of subsonic open cavity flow fields, Phys. Fluids 21 (2009), https://doi.org/10.1063/1.3210772.
[25] A. Nekkanti, O.T. Schmidt, Frequency–time analysis, low-rank reconstruction and denoising of turbulent flows using spod, J. Fluid Mech. 926 (2021) A26, https://doi.org/10.1017/jfm.2021.681.
[26] A. Nekkanti, O.T. Schmidt, Gappy spectral proper orthogonal decomposition, J. Comput. Phys. 478 (2023) 111950, https://doi.org/10.1016/j.jcp.2023.111950.
[27] S. Nidhan, K. Chongsiripinyo, O.T. Schmidt, S. Sarkar, Spectral proper orthogonal decomposition analysis of the turbulent wake of a disk at re = 50 000, Phys. Rev. Fluids 5 (2020) 124606, https://doi.org/10.1103/PhysRevFluids.5.124606.
[28] B.R. Noack, K. Afanasiev, M. Morzyński, G. Tadmor, F. Thiele, A hierarchy of low-dimensional models for the transient and post-transient cylinder wake, J. Fluid Mech. 497 (2003) 335–363, https://doi.org/10.1017/S0022112003006694.
[29] M. Oliver, R. Webster, Kriging: a method of interpolation for geographical information systems, Int. J. Geogr. Inf. Syst. 4 (1990) 313–332, https://doi.org/10.1080/02693799008941549.
[30] L. Rego, F. Avallone, D. Ragni, D. Casalino, Jet-installation noise and near-field characteristics of jet–surface interaction, J. Fluid Mech. 895 (2020), https://doi.org/10.1017/jfm.2020.294.
[31] J. Rossiter, Wind tunnel experiments on the flow over rectangular cavities at subsonic and transonic speeds, in: ARC 26621, vol. 3438, Ministry of Aviation, 1964.
[32] C. Rowley, S. Dawson, Model reduction for flow analysis and control, Annu. Rev. Fluid Mech. 49 (2017) 387–417, https://doi.org/10.1146/annurev-fluid-010816-060042.
[33] I. Scherl, B. Strom, J. Shang, O. Williams, B. Polagye, S. Brunton, Robust principal component analysis for modal decomposition of corrupt fluid flows, Phys. Rev. Fluids 5 (2020), https://doi.org/10.1103/PhysRevFluids.5.054401.
[34] O. Schmidt, A. Towne, G. Rigas, T. Colonius, G. Brès, Spectral analysis of jet turbulence, J. Fluid Mech. 855 (2018), https://doi.org/10.1017/jfm.2018.675.
[35] O.T. Schmidt, Spectral proper orthogonal decomposition using multitaper estimates, Theor. Comput. Fluid Dyn. 36 (2022) 741–754, https://doi.org/10.1007/s00162-022-00626-x.
[36] O.T. Schmidt, T. Colonius, Guide to spectral proper orthogonal decomposition, AIAA J. 58 (2020) 1023–1033, https://doi.org/10.2514/1.J058809.
[37] S. Singh, L. Ukeiley, Proper orthogonal decomposition of high-speed particle image velocimetry in an open cavity, AIAA J. 5 (2020) 2975–2990, https://doi.org/10.2514/1.j059046.
[38] A. Solera-Rico, C. Sanmiguel Vila, M. Gómez-López, Y. Wang, A. Almashjary, S.T.M. Dawson, R. Vinuesa, *b*-variational autoencoders and transformers for reduced-order modelling of fluid flows, Nat. Commun. 15 (2024), https://doi.org/10.1038/s41467-024-45578-4.
[39] Y. Sun, Q. Liu, L.N. Cattafesta, L.S. Ukeiley, K. Taira, Resolvent analysis of compressible laminar and turbulent cavity flows, AIAA J. 58 (2020) 1046–1055, https://doi.org/10.2514/1.J058633.
[40] Y. Sun, K. Taira, L.N. Cattafesta, L.S. Ukeiley, Biglobal instabilities of compressible open-cavity flows, J. Fluid Mech. 826 (2017) 270–301, https://doi.org/10.1017/jfm.2017.416.
[41] K. Taira, S. Brunton, S. Dawson, C. Rowley, T. Colonius, B. McKeon, O. Schmidt, S. Gordeyev, V. Theofilis, L. Ukeiley, Modal analysis of fluid flows: an overview, AIAA J. 55 (2017) 4013–4041, https://doi.org/10.2514/1.J056060.
[42] A. Towne, O.T. Schmidt, T. Colonius, Spectral proper orthogonal decomposition and its relationship to dynamic mode decomposition and resolvent analysis, J. Fluid Mech. 847 (2018) 821–867, https://doi.org/10.1017/jfm.2018.283.
[43] D. Venturi, G. Karniadakis, Gappy data and reconstruction procedures for flow past a cylinder, J. Fluid Mech. 519 (2004) 315–336, https://doi.org/10.1017/S0022112004001338.
[44] J.G.R. Von Saldern, J.M. Reumschüssel, T.L. Kaiser, M. Sieber, K. Oberleithner, Mean flow data assimilation based on physics-informed neural networks, Phys. Fluids 34 (2022), https://doi.org/10.1063/5.0116218.
[45] J. Westerweel, F. Scarano, Universal outlier detection for piv data, Exp. Fluids 39 (2005) 1096–1100, https://doi.org/10.1007/s00348-005-0016-6.
[46] M. Wilczek, R.J.A.M. Stevens, C. Meneveau, Spatio-temporal spectra in the logarithmic layer of wall turbulence: large-eddy simulations and simple models, J. Fluid Mech. 769 (2015) R1, https://doi.org/10.1017/jfm.2015.116.
[47] X. Yuan, J. Yang, Sparse and low rank matrix decomposition via alternating direction method, Pac. J. Optim. 9 (2009).
[48] Y. Zhang, Y. Sun, N. Arora, L.N. Cattafesta III, K. Taira, L.S. Ukeiley, Suppression of cavity flow oscillations via three-dimensional steady blowing, AIAA J. 57 (2019) 90–105, https://doi.org/10.2514/1.J057012.
[49] E. Özalp, G. Margazoglou, L. Magri, Reconstruction, forecasting, and stability of chaotic dynamics from partial data, Chaos, Interdiscip. J. Nonlinear Sci. 33 (2023), https://doi.org/10.1063/5.0159479.